# Experimental Observation of Redox-Induced Fe−N Switching Behavior as a Determinant Role for Oxygen Reduction Activity

Qingying Jia,[†] Nagappan Ramaswamy,[†,⊥] Hasnain Hafiz,[‡] Urszula Tylus,[†,∥] Kara Strickland,[†] Gang Wu,[∥,#] Bernardo Barbiellini,[‡] Arun Bansil,[‡] Edward F. Holby,[§] Piotr Zelenay,[∥] and Sanjeev Mukerjee*,[†]

[†]Department of Chemistry and Chemical Biology, and [‡]Department of Physics, Northeastern University, Boston, Massachusetts 02115, United States and [§]Materials Science and Technology Division, and [∥]Materials Physics and Applications Division, Los Alamos National Laboratory, Los Alamos, New Mexico 87545, United States. [⊥]Present address: Global Fuel Cell Activities, General Motors Corporation, Pontiac, MI 48340, United States. [#]Present address: Department of Chemical and Biological Engineering, University at Buffalo, The State University of New York, Buffalo, NY 14260, United States.

ABSTRACT The commercialization of electrochemical energy conversion and storage devices relies largely upon the development of highly active catalysts based on abundant and inexpensive materials. Despite recent achievements in this respect, further progress is hindered by the poor understanding of the nature of active sites and reaction mechanisms. Herein, by characterizing representative iron-based catalysts under reactive conditions, we identify three Fe−N$_4$-like catalytic centers with distinctly different Fe−N switching behaviors (Fe moving toward or away from the N$_4$-plane) during the oxygen reduction reaction (ORR), and show that their ORR activities are essentially governed by the dynamic structure associated with the Fe$^{2+/3+}$ redox transition, rather than the static structure of the bare sites. Our findings reveal the structural origin of the enhanced catalytic activity of pyrolyzed Fe-based catalysts compared to nonpyrolyzed Fe-macrocycle compounds. More generally, the fundamental insights into the dynamic nature of transition-metal compounds during electron-transfer reactions will potentially guide rational design of these materials for broad applications.
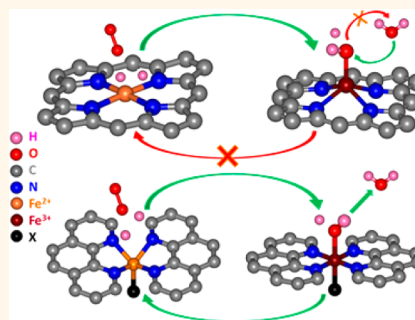
KEYWORDS: non-PGM catalysts · oxygen reduction reaction · active sites · redox transition · dynamic structure

The development of non-platinum group metal (non-PGM) catalysts for oxygen reduction reaction (ORR), especially in acidic media, constitutes one of the grand challenges in materials discovery for electrochemical energy conversion and storage. Among a broad variety of non-PGM catalysts that have been explored, a class of catalysts comprising transition metal ions stabilized by nitrogen functional groups on carbonaceous surfaces (M−N$_x$−C, M= Co or Fe) are most promising as they have demonstrated ORR activity and stability approaching those of commercial Pt/C catalysts.[1−3] Further progress, which is necessary for M−N$_x$−C catalysts to become viable, requires proper understanding of the nature of active sites and the underlying mechanistic principles governing catalytic activity. In accordance to Sabatier's principle,[4] the high ORR activity of M−N$_x$−C active sites is likely attributed to the moderate adsorption strength between the active sites and the key ORR intermediates, which is justified by recent success in extending the linear scaling relations between the adsorption energies of different reaction intermediates to various transition-metal compounds including M−N$_x$−C moieties.[5] Meanwhile, many studies[6−8] have shown that the ORR activity (especially the onset potential) of M−N$_x$−C moieties is directly related by the redox potential of M. We show here that the adsorption strength between the identified Fe−N$_x$−C active sites and ORR intermediates are primarily determined by the structure changes associated with the Fe$^{2+/3+}$ redox transition, thereby unifying the two arguments.

The structures of active sites in high-temperature treated M−N$_x$−C catalysts have been extensively studied since it was discovered that such a treatment leads to

significant increase in ORR activity and stability.[9,10] Though no consensus has been reached in this regard, $M-N_x$ moieties embedded in the defects and/or interstices of graphitic sheets have been repeatedly identified in both M-macrocycle-pyrolyzed catalysts[11−13] and $M-N_x-C$ synthesized from individual M, N, and C precursors.[14−16] The location of this site on carbon (edge versus basal plane),[6,17,18] the coordination number ($M-N_4$ vs non$-M-N_4$),[14,16,19] the number of M atoms,[19,20] and the functional nitrogen type (pyridinic, pyrrolic, graphitic)[21] are still under extensive debate. Recently, a new active site with the Fe^{2+} locating out of the N_4-plane toward a fifth axial ligand was proposed to have exceptional intrinsic activity, and be responsible for the high activity of the current state-of-the-art $Fe-N_x-C$ catalysts.[14] Meanwhile, the highest theoretical ORR activity for any non-PGM catalyst structure heretofore was reported on the Fe_2N_5(*OH) site in which the Fe is also 5-coordinate and located out of the graphene plane.[20] However, the existence of such 5-coordinate sites in pyrolyzed $Fe-N_x-C$ catalysts has not been verified, and the structural origin of its high catalytic activity is also unclear.

Previous efforts to characterize $M-N_x-C$ active sites have mainly focused on the local geometry of the sites free of adsorbates, whereas the structural changes induced by adsorption/desorption of reaction intermediates, which plays a major role for the catalytic activity of transition-metal compounds (such as those in biological systems[22]), remain unexplored. Here, we fill that knowledge gap by providing the first experimental evidence for dissimilar Fe−N switching behaviors of different active sites during ORR, which are responsible for their different ORR activities. This is achieved by conducting synchrotron-based *in situ* X-ray absorption spectroscopy (XAS) studies of iron *meso*-tetraphenylporphyrine chloride (FeTPPCl) pyrolyzed at various temperatures and a state-of-the-art PANI−Fe−C catalyst.[2] The former represents a class of catalyst derived from precursors with existing heme coordinated $Fe-N_4$ moiety and the latter, a class of catalyst where the active site is created during pyrolysis of composites derived from the individual precursors of Fe, N, and C. Changes of the bond distance, coordination number, iron oxidation state, and adsorbed oxygen species coverage as a function of applied potential are monitored using a combination of extended X-ray absorption fine structure (EXAFS), X-ray absorption near edge structure (XANES), and $\Delta\mu$ analysis. This, along with the *ab initio* FEFF9[23] and density functional theory (DFT) calculations, provides unique insight into the active site geometry and structural transition during ORR, which are essential in designing future non-PGM catalysts.

RESULTS AND DISCUSSION

Fe−N Switching Behavior during ORR. It is known that the original porphyrin macrocycle possesses a square-planar

$Fe^{2+}-N_4$ structure (D_{4h} symmetry), and the Fe^{2+}-center shifts out of the plane toward the O(H)$_{ads}$ (adsorbed O* and/or OH*) species when (H)O$-Fe^{3+}-N_4$ is formed.[6,24,25] This Fe−N switching behavior is illustrated by the XAS spectra of FeTPP-300-C (FeTPP pyrolyzed at 300 °C) collected at a potential ranging from 0.1 to 0.9 V in N_2-saturated 0.1 M KOH electrolyte (Figure 1a and b). The Fe K-edge XANES at 0.1 V closely resembles that of the pre-existing porphyrin macrocycle. In particular, the shoulder at 7117 eV is the fingerprint of the square-planar $Fe-N_4$ structure.[26] As the potential increases from 0.1 to 0.9 V the Fe K-edge shifting toward higher energy is indicative of the Fe^{2+}/Fe^{3+} redox transition.[6,26] Concurrently, the Fourier transform (FT) peak at ∼1.6 Å arising from the Fe−N/O scattering increases in intensity and shifts to a larger radial distance. The corresponding increases in Fe-centered coordination number (Figure 1c) and bond distance (Figure 1d) caused by O(H)$_{ads}$ are confirmed by EXAFS fitting (Supporting Information Figure S1). The XAS spectra of FeTPP-300-C collected in N_2-saturated 0.1 M $HClO_4$ exhibit essentially the same trends, except that some of the $Fe-N_4$ moieties are already oxidized at 0 V due to the lower Fe^{2+}/Fe^{3+} redox potential at low pH (Supporting Information Figure S2), and therefore the Fe^{2+}/Fe^{3+} redox transition is not fully captured as in 0.1 M KOH electrolyte.

The same analysis was also conducted with FeTPP-800-C and PANI−Fe−C catalysts, for which the structure of the active site is unclear. Interestingly, the XAS spectra of the two catalysts collected in N_2-saturated 0.1 M $HClO_4$ exhibit the similar trends as observed on FeTPP-300-C: the Fe K-edge shifts toward higher energy with increasing potential, accompanied by the increase in Fe−N/O scattering peak intensity (Figure 1a and b). This indicates that the active sites in these catalysts also undergo a Fe^{2+}/Fe^{3+} redox transition that triggers the adsorption of *OH from water activation, but at much higher potentials (∼0.7 V). It is noted that the spectra of all catalysts obtained in N_2- and O_2-saturated electrolyte at the same potential are within experimental uncertainties. This implicates that the Fe^{2+}-sites are poisoned by the O(H)* from water activation above the redox potential, which is consistent with our previous observation that the Fe^{2+}/Fe^{3+} redox potential overlaps with the ORR onset potential.[7] The higher Fe^{2+}/Fe^{3+} redox potential of pyrolyzed Fe-based catalysts compared to that of original $Fe-N_4$ macrocycles to a large extent accounts for the enhanced ORR activity via stabilization of active Fe^{2+}-sites at higher potentials. It is thus of particular importance to elucidate the structural origin and changes accompanying the redox potential increase, with apparent concomitant decrease in Fe−O binding energy.

A key difference in the active site structure within these catalysts lies in the average Fe−N bond distance (R_{Fe-N}). The R_{Fe-N} in PANI−Fe−C is much longer than
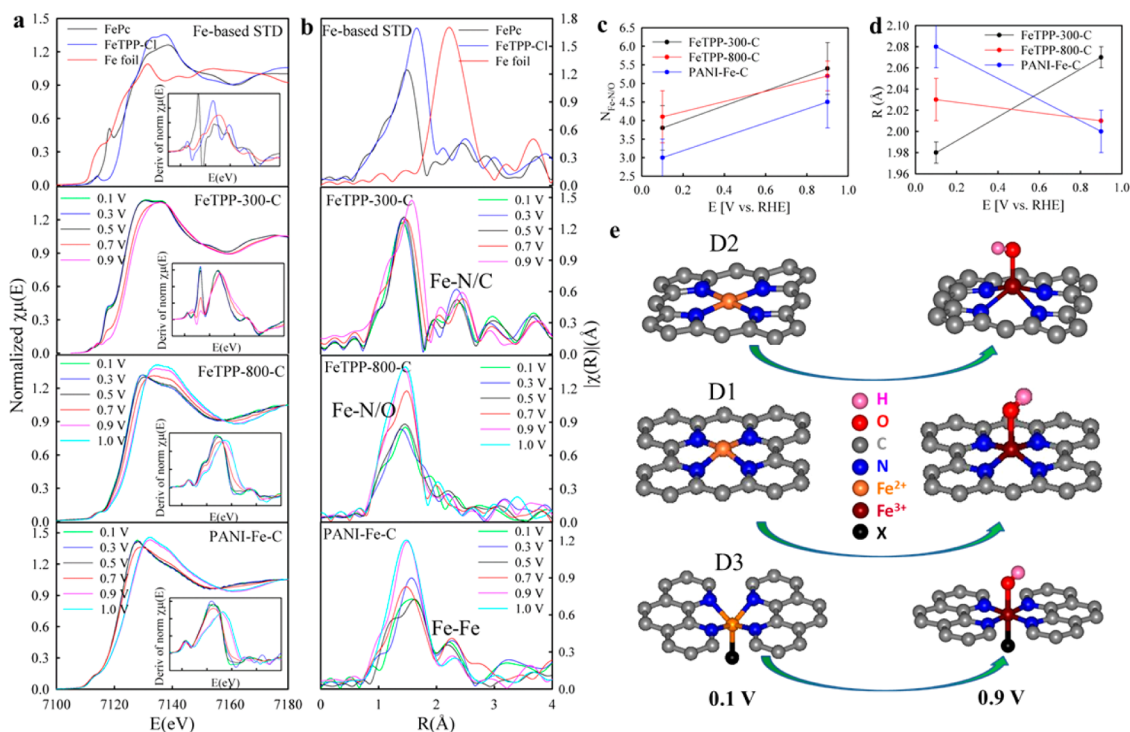
Figure 1. (a) XANES at the Fe K-edge with concomitant first derivatives (insets). (b) the corresponding FT-EXAFS of FeTPP-300-C, FeTPP-800-C, and PANI−Fe−C as a function of applied potentials versus reversible hydrogen electrode. XANES and FT-EXAFS spectra of iron(II) phthalocyanine (FePc), iron(III) *meso*-tetraphenyl porphyrin chloride (FeTPPCl), and bulk iron (top) were included as Fe-based standards for comparison. The spectra of FeTPP-800-C and PANI−Fe−C were collected in N_2-saturated 0.1 M $HClO_4$ electrolyte; while the spectra of FeTPP-300-C collected in N_2-saturated 0.1 M KOH electrolyte is displayed here to fully capture the Fe^{2+}/Fe^{3+} redox transition. The Fe−N/O (N and O cannot be distinguished by XAS as surrounding atoms) coordination numbers (c) and bond distances (d) of FeTPP-300-C, FeTPP-800-C, and PANI−Fe−C at 0.1 and 0.9 V vs reversible hydrogen electrode (RHE) were obtained by EXAFS fits, and the derived Fe−N switching behavior is illustrated by three structural models (Fe−N_4−C_x) labeled as D2, D1, and D3, respectively, with/without axially bound $O(H)_{ads}$ (e). The atom labeled X represents the fifth ligand with its identity unknown. The vertical error bars in (c) and (d) are produced by the fitting software (full details can be found in Supporting Information Table S2).

that in FeTPP-300-C at 0.1 V, but shorter at 0.9 V (Figure 1c). The shortening of $R_{Fe−N}$ in PANI−Fe−C with increasing potential suggests that the central Fe^{2+} in PANI−Fe−C is initially out of the plane and moves back toward plane upon the formation of axially bound $O(H)_{ads}$ (Figure 1e bottom), contrary to the Fe−N switching behavior observed on FeTPP-300-C (Figure 1e top). The value of $R_{Fe−N}$ in FeTPP-800-C does not change much with potential, remaining mildly larger than that in FeTPP-300-C at 0.1 V. This suggests the minimal structural change during ORR with a mild displacement (Figure 1e middle).

The nonplanar Fe−N_x-C structure in pyrolyzed Fe-based catalysts is further substantiated by comparing the experimental XANES data to the theoretical results calculated using the *ab initio* FEFF9. The XANES spectra of all the catalysts at 0.1 V possess the characteristic features (labeled as A-E) of analogue Fe-centered macrocycles (Figure 2a),[27−30] which are well captured by the multiple scattering FEFF9 calculations based on Fe−N_4-C_x models (Figure 2b). All these features exhibit monotonic trends in amplitude and/or position as the catalysts are ordered in the ascending Fe−N bond distance: the intensities of features A and C increase

and of features B and D decrease, and feature E shifts toward lower energy. Most interestingly, all these trends can be well reproduced in theoretical XANES by gradually moving the central Fe away from the N_4-plane (Figure 2b), and fully accounted for by the distortion of the D_{4h} symmetry and the increase in $R_{Fe−N}$ as a consequence of the Fe displacement (see the Supporting Information for a more detailed discussion). In particular, the position of feature E relative to the threshold energy (ΔE) is coupled to the mean first shell metal−ligand bond length (R), as governed by Natoli's rule:[31] $\Delta E \times R^2 =$ constant. Thus, feature E shifting toward lower energy directly reflects the increase in $R_{Fe−N}$. Likewise, the comparison of the feature E position in the spectra collected at 0.9 V clearly shows that the $R_{Fe−N/O}$ in FeTPP-800-C and PANI−Fe−C is shorter than in FeTPP-300-C (Supporting Information Figure S5). The excellent agreement between the experimental and theoretical results unambiguously demonstrates the distinct Fe displacement and Fe−N switching behavior presented by the three representative catalysts, and the Fe−N−C active sites formed upon high temperature pyrolysis exhibited distorted Fe−N_x local structures featured
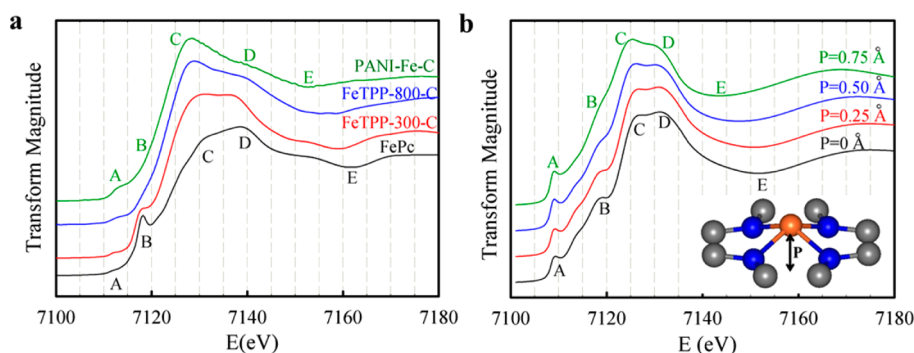
Figure 2. (a) Catalyst XANES spectra collected at 0.1 V in N_2-saturated 0.1 M $HClO_4$; the XANES of bulk FePc as a square-planar Fe^{2+}-N_4 standard is included. (b) XANES spectra calculated by FEFF9 based on the Fe−N_4-C_8 model (inset) with various central Fe displacements (denoted as P). Note the change of the relative intensity of features C and D.

with Fe displacements and elongated Fe−N bond distance.

The Nature of Active Sites. By employing the surface sensitive $\Delta\mu$ technique, we showed previously that the active site in FeTPP-300-C in alkaline solution is well represented by a Fe−N_4−C_{12} cluster model inscribed in the original iron-porphyrin macrocycle cavity (denoted hereafter as D2, based on the symbol commonly used in Mössbauer studies[14,15]), while the majority of the active sites in FeTPP-800-C are well represented by an Fe−N_4−C_{10} site with Fe positioned in a C-divacancy in the basal plane and/or an Fe−N_4−C_8 cluster model in the armchair edges of graphitic surfaces (denoted as D1 hereafter).[6] The $\Delta\mu$ signals obtained from FeTPP-300-C and FeTPP-800-C in acid (Supporting Information Figure S4) are essentially the same as those obtained in alkaline,[6] indicating similar active sites in different pH environments. The commonality of the role of the active site at the two extreme ends of the pH scale has been extensively discussed in the context of one of the catalysts studied in this work, that is, FeTPP,[6,32] that in both pH environments the reactions mediated by Fe-sites occur through inner-sphere charge transfer process. The Fe−N_4 coordination in FeTPP-300-C and FeTPP-800-C is also supported by EXAFS fits (Supporting Information Table S1).

Unlike the FeTPP-pyrolyzed catalysts, the PANI−Fe−C exhibits two FT peaks (Figure S1 bottom right) even under *in situ* acidic conditions. The second FT peak at ∼2.1 Å can be well fitted as a Fe−Fe scattering with a bond length of ∼2.54 Å, which is close to the Fe−Fe bond length in bulk iron (2.49 Å) or iron carbide (2.48 Å). Attempts to fit this peak as C, N, O, or S interaction with Fe, gave poorer fits and refinements and led to physically unreasonable coordination, and/or Debye−Waller factors. This indicates that PANI−Fe−C contains some metallic iron that is stable under the acidic environment; this is ascribed to the protection by the surrounding onionlike graphitic carbon nanoshells as directly observed by high-resolution transmission electron microscopy (HRTEM).[2] Recently,

it was proposed that the metallic iron encapsulated in carbon nanotubes[33] or graphitic layers[34,35] may be a new active site for ORR, but it is beyond the scope of this work. The Fe−N coordination number ($N_{Fe−N}$ = 3.0) for PANI−Fe−C is a weighted average of the $N_{Fe−N}$ in the Fe−N_x moieties ($N_{Fe−N}$ = x) and in the metallic iron ($N_{Fe−N}$ = 0) owing to the bulk nature of EXAFS, and is thus smaller than x. As the metallic iron content is relatively low as suggested by the small $N_{Fe−Fe}$, the x is not expected to exceed 3.0 by much, pointing to the Fe−N_4 and/or Fe−N_5 moieties in PANI−Fe−C.

To reveal how D1 is formed in FeTPP catalysts during pyrolysis, the FeTPPCl pyrolyzed at various temperatures has been investigated by combining XAS and rotating disk electrode (RDE) methods. The XANES evolution trend of the FeTPP-pyrolyzed catalysts displayed in Figure 3a confirms the Fe displacement increase with increasing pyrolysis temperature, which is expected for increasing D1(nonplanar) concentration *vs* that of the pre-existing D2 (planar) as pyrolysis temperatures are increased. Consistent with the XAS results, square-wave voltammetry profiles of these catalysts (Figure 3b) show the reduction in the redox peak intensity of D2 at ∼0.15 V and the concurrent increase in the redox peak intensity of D1 at ∼0.75 V with increasing pyrolysis temperature. The increasing ORR activity trend (Figure 3b, inset) with increasing D1 content clearly shows that D1 is responsible for the higher activities of these catalysts, despite the coexistence of D1 and D2 sites in the pyrolyzed FeTPP samples. The diminishing of the FT peaks (∼2.5 Å) that arise from the carbon atoms in the second shell of the pre-existing macrocycle for FeTPP-800-C (Figure 3c) suggests that the Fe−N_4 moiety is detached from D2 upon high-temperature treatment, and recaptured at divacant defective centers and/or edge-plane sites on the amorphous carbon support forming D1. The shoulder at 7117 eV (feature B) becomes indiscernible in the XANES of FeTPP-800-C, but is visible in the first derivative of the XANES (Figure 1a, inset). This indicates some residual D2 sites in FeTPP-800-C, consistent with the weak redox peak of D2 at ∼0.15 V (Figure 3c).
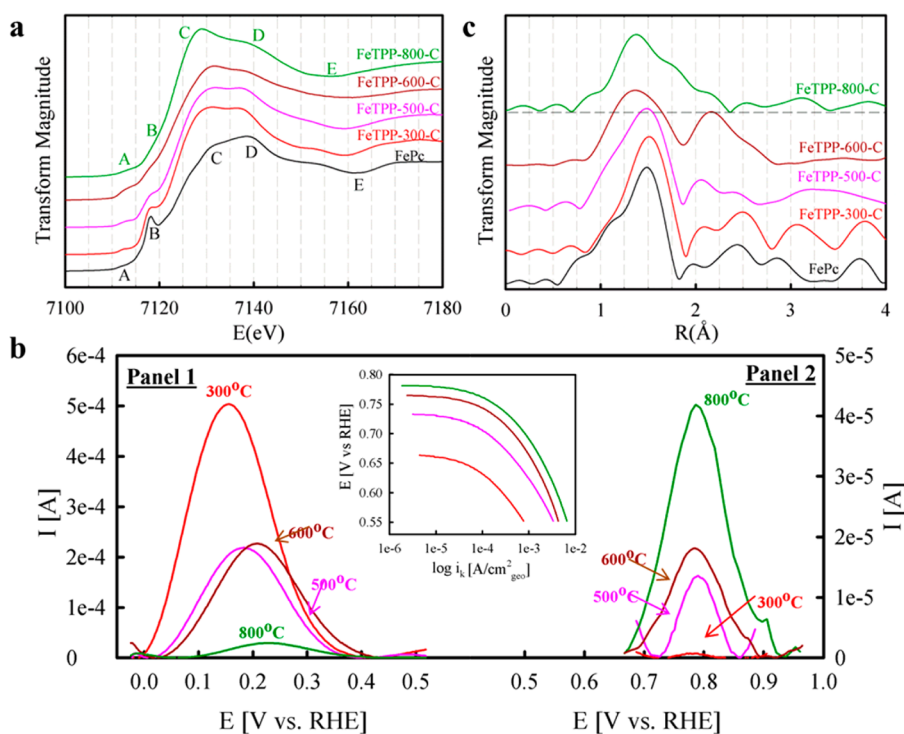
Figure 3. XANES (a) and FT-EXAFS (b) of FeTPP-pyrolyzed dry powders (except for FeTPP-800-C) together with the bulk FePc; the spectra of FeTPP-800-C were collected at 0.1 V in N_2-saturated 0.1 M $HClO_4$ electrolyte. (c) Square wave voltammetry (SWV) profiles of FeTPP-pyrolyzed catalysts as a function of pyrolysis temperature. All SWV experiments were performed in N_2-saturated 0.1 M $HClO_4$ electrolyte with a step potential of 5 mV, amplitude of 20 mV, and scan frequency of 10 Hz. Note that the scaling for the left and right current axes is different. The ORR activity trend of the FeTPP-pyrolyzed catalysts is illustrated by the Tafel plots (inset) obtained from RDE experiments in O_2-saturated 0.1 M $HClO_4$ electrolyte at 900 rpm and 20 mV·s^{-1} scan rate.

Further increase of the pyrolysis temperature leads to the decrease of the ORR activity, with the product dominated by inactive metallic iron and/or iron oxides (Supporting Information Figure S3).[6]

The XAS results are generally consistent with Mössbauer characterization of Fe-macrocycle-pyrolyzed catalysts, which allow for the identification of two types of Fe−N_4 moieties and metallic iron (oxides) in various proportions, depending on the pyrolysis temperature. They are assigned to the square-planar Fe−N_4 in medium-spin state (MS) and low-spin state (LS) in the original macrocycle (D2) and Fe−N_4 embedded in carbon support (D1), respectively.[9,12,13,36] The discrepancy regarding the central Fe position in D1 between the *ex situ* Mössbauer and *in situ* XAS results is likely caused by the structure modifications of the sites upon contact with an electrolyte solution. A recent DFT study[20] suggests that the binding of *OH occurs spontaneously in aqueous environments on an Fe_2N_5 C-edge site, leading to a new active site with higher catalytic activity. Similarly, Yeager *et al.* believed[37] that the active sites are not formed during the heat-treatment of M-N_4 chelates, but upon contact with solutions afterward.

D1 was also found in PANI−Fe−C[38] and many other Fe−N_x−C catalysts synthesized using individual Fe, N, and C precursors,[14,15] but the Fe−N_4 moieties in PANI−Fe-C may also be located in the micropores derived from the highly microporous carbon material, in addition to the edges/defects of graphene sheets. As the average Fe−N bond distance ($R_{Fe−N}$) in PANI−Fe−C (2.08 ± 0.02 Å) is longer than that in the D1 dominated FeTPP-800-C (2.03 ± 0.02 Å), PANI−Fe−C must contain some Fe−N_x species with the $R_{Fe−N}$ longer than 2.08 Å. This long Fe−N bond distance is often coupled to a high-spin (HS) Fe^{2+} ion located out of the graphene plane[22] with a fifth axial ligand required for stabilization. Previous Mössbauer studies also suggested a Fe^{2+}(HS)−N_4 site in PANI−Fe−C with the central Fe bonding to axial ligand(s).[38] This structure resembles those of the noncoplanar N_{axi}−Fe^{2+}(HS)−N_4 site in myoglobin[22] or other biomimetic catalysts.[39] Interestingly, myoglobin exhibits the same Fe−N switching behavior observed on PANI−Fe−C: the Fe^{2+}-center shifts back toward the plane upon the formation of axially bound species.[22] These results together strongly indicate the existence of the fifth axial ligand at this site despite the lack of direct observation. A similar nonplanar NH_2−Fe^{2+}(HS)−N_4 site (denoted as D3) was proposed by Dodelet *et al.* in pyrolyzed Fe−N_x−C catalysts.[14] However, this work provides the first experimental evidence for the substantial Fe^{2+}-center displacement with elongated Fe−N bonds, and suggests the presence of the fifth
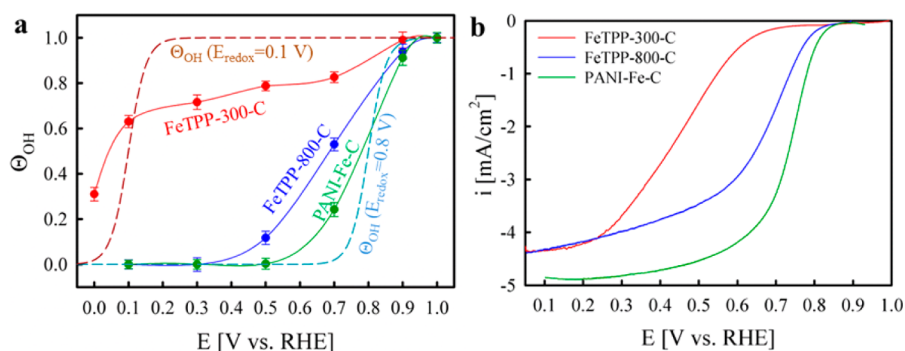
Figure 4. (a) Experimental $\Theta_{OH}(s)$ as a function of potential extracted from the $\Delta\mu$ data in Supporting Informationy Figure S4, in comparison to the two calculated $\Theta_{OH}(s)$ based on eq 3 using the redox potential of 0.05 or 0.85 V, respectively, and the temperature of 298 K. (b) ORR polarization curves obtained in O_2-saturated 0.1 M $HClO_4$ electrolyte at 900 rpm rotation rate and 20 mV·s^{-1} scan rate. Note the ORR polarization curve of PANI–Fe–C presented previously[2] was obtained using a different testing protocol, and is not identical to that shown here. Vertical error bars in (a) refer to errors involved in determining Θ_{OH} from multiple experimental scans collected at each potential.

ligand as the cause of the significant Fe displacement. In addition, we demonstrate that the Fe–N switching behavior of the D3 site during ORR is opposite to that of the pre-existing macrocycle (D2) as represented by FeTPP-300. This accounts primarily for the exceptional inherent activity in terms of turnover frequency (TOF) that far exceeds the TOFs of D1 and D2 sites.[14] Given that FeTPP-800 contains D1 and D2 sites while PANI–Fe–C contains D1 and D3 sites, the superior inherent activity of PANI–Fe–C to that of FeTPP-800 is likely attributed to D3 sites.

Structural Origin of Enhanced ORR Activity. As revealed by the combined *in situ* EXAFS, XANES, and $\Delta\mu$ analysis, all three types of active sites considered undergo the Fe^{2+}/Fe^{3+} redox transition with the denouement of the Fe^{3+} associated with the adsorption of *OH through water activation:

$$N_x-Fe^{2+} + H_2O \rightarrow N_x-Fe^{3+}-OH_{ads} + H^+ + e^- \quad (1)$$
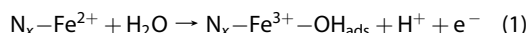
Such transition was previously predicted by Anderson *et al.*[40] as the potential determining step (pds) for Fe–N_4-based sites with a reversible potential (V_{pds}) of 0.64 V based on theoretical computations. The model however was simplistic with Fe–N_4 without any carbon embodiments. The difference between V_{pds} and the ORR reversible potential (1.23 V) represents a thermodynamic overpotential as potentials higher than V_{pds} have a thermodynamic barrier between intermediate reaction states.[41] We show below that the ORR activity of Fe-based catalysts is closely related to the $O(H)_{ads}$ coverage, suggesting that the desorption of oxygenated adsorbates is controlling the overall activity.

The change in $O(H)_{ads}$ coverage on Pt electrodes with applied potential can be best followed by plotting the $\Delta\mu$ magnitude ($|\Delta\mu|$) as a function of potential.[42,43] In the Fe–N_x–C case, the negative dip centered at 7126 eV in the $\Delta\mu$ spectra reflects the charge transfer from the metal center to adsorbed oxygen species.[44] The increase in $|\Delta\mu|$ with increasing potential up to

1.0 V (Supporting Information Figure S4) indicates that the Fe^{2+}-sites are progressively occupied by $O(H)_{ads}$ until reaching occupancy saturation at 1.0 V. The relative $O(H)_{ads}$ coverage (Θ_{OH}) at a potential E is thus represented by the ratio of $|\Delta\mu_E|/|\Delta\mu_{1.0V}|$. Potential dependence of Θ_{OH} shown in Figure 4a clearly shows that $O(H)_{ads}$ starts to occupy the active sites at potentials far below the ORR onset potential for all considered catalysts (Figure 4b), and tracks measured current densities. These results point to a surface redox mediated electrocatalytic process with potential-dependent population of active sites, for which the population of active sites and the reaction rate can be expressed as[45]

$$N_{active} = N_{total} \frac{1}{1 + e^{F/RT(E - E_{redox})}} \quad (2)$$

$$\Theta_{O^*} = \frac{N_{total} - N_{active}}{N_{total}} = \frac{1}{1 + e^{-F/RT(E - E_{redox})}} \quad (3)$$

$$J \propto N_{total}(1 - \Theta_{O^*}) \exp\left(-\frac{\Delta H^*}{RT}\right) \exp\left(-\frac{E - E^0}{b}\right) \quad (4)$$

where N_{active} and N_{total} are the available and total number of surface active sites, respectively; F is the Faraday constant; R is the universal gas constant; T is the temperature; E is the cathode potential; E_{redox} is the redox potential under the relevant operation conditions; Θ_{O^*} is the coverage by adsorbed oxygen species at potential E; ΔH^* is the activation energy for the electrocatalytic process; E^0 is the standard potential for the faradaic process; and b is the value of the Tafel slope. The general trend between Θ_{OH} and measured current density manifested in Figure 4 illustrates the site blocking effect that lies in the pre-exponential factor $(1 - \Theta_{O^*})$ of the rate expression (eq 4). The rising curves of the experimental $\Theta_{OH}(s)$ overall follow the theoretical $\Theta_{OH}(s)$ derived from eq 3, which suggests that the surface coverage of oxygen species is governed by the cathode potential relative to the redox potential. The gradual slopes observed in experimental $\Theta_{OH}(s)$

implicate multiples types of active sites and/or poor kinetics of the catalysts. Some important conclusions can be derived from the qualitative analysis: (i) the catalytically active sites are $Fe^{2+}-N_x$ rather than $Fe^{3+}-N_x$ sites; (ii) the ORR rate mediated by $Fe^{2+}-N_x$ sites is limited by the removal of oxygen species; (iii) the cathode potential needs to be sufficiently negative to generate enough $Fe^{2+}-N_x$ sites to proceed ORR, accounting for the previously observed strong correlation between the $Fe^{2+/3+}$ redox potential and ORR onset potential;[7] and (iv) positive shift of $Fe^{2+/3+}$ redox potential resulting in stabilization of active $Fe^{2+}-N_x$ sites at elevated potentials, thereby promoting ORR. A quantitative analysis of Θ_{OH} as a function of applied and redox potential on the basis of multiple sites is currently under preparation. This, in addition to the *in situ* real-time XAS measurements of Θ_{OH} at short and long time scales, is expected to give a comprehensive understanding of the nature of various active sites and the structural origins of their activity and durability toward ORR.

Following observation that greater Fe displacement (or longer Fe−N bond) leads to lower $O(H)_{ads}$ coverage and higher ORR activity of studied catalysts, DFT calculations were performed to investigate the effects of the Fe displacement on the electronic property of $Fe-N_4-C_{x-}$ sites and its binding energies with ORR intermediates. The DFT conducted here disregards the solvation and entropic effects but is sufficient for comparing relative activities and predicting limiting steps in the ORR reaction pathway as shown by different research groups.[20,46,47] The different Fe−N switching behaviors exhibited by FeTPP-300-C, FeTPP-800-C, and PANI−Fe−C are nicely reproduced by $Fe-N_4-C_{12}$ (D2), $Fe-N_4-C_{10}$ (D1), and $N_{axi}-Fe-N_4-C_8$ (D3) models, respectively (Supporting Information Figure S7 and Table S3). The overbinding of $O(H)_{ads}$ on the three sites as suggested by the experimental results is manifested by their free energy diagrams (Supporting Information Figure S8). Most importantly, the addition of an axial NH_2 ligand to the $Fe-N_4-C_8$ model (forming $N_{axi}-Fe-N_4-C_8$) results in the reverse of the Fe−N switching behavior, and the decrease of the binding energies of ORR intermediates (Supporting Information Table S4), thereby drastically increasing the ORR activity as manifested by the calculated reaction pathways (Figure 5a). Correspondingly, the V_{pds} is significantly increased from −0.18 to 0.73 V, close to the highest calculated value (0.80 V) of V_{pds} for any non-PGM catalyst structure to date.[20] Once the applied potential exceeds the V_{pds}, water activation (eq 1) becomes downhill in energy or exothermic (Figure 5b), and the produced oxygen species poison the surface $Fe^{2+}-N_x$ active sites. This agrees with the experimental observation of the adsorption of *OH from water activation triggered by Fe^{2+}/Fe^{3+} redox transition. In accordance with our results, the record high V_{pds} obtained on the $FeCoN_5$(*OH) site is essentially triggered by the binding of an *OH as a

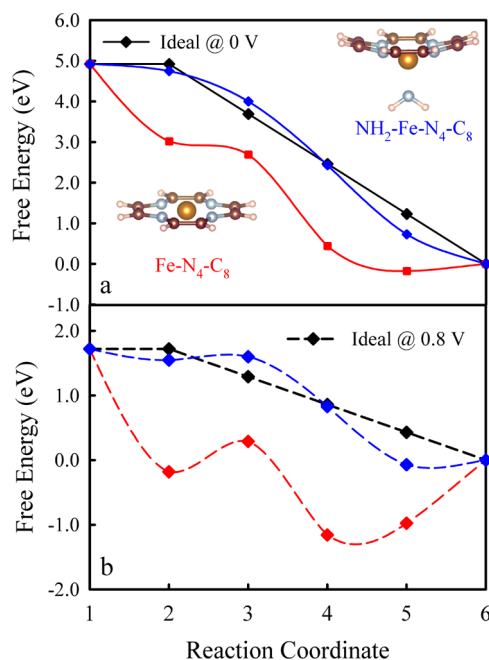**Figure 5.** Reaction coordinates correspond to the given systems: (1) *$+O_2 + 4H^+ + 4e^-$, (2) *$OO + 4H^+ + 4e^-$, (3) *$OOH + 3H^+ + 3e^-$, (4) *$O + 2H^+ + 2e^- + H_2O$, (5) *$OH + H^+ + e^- + H_2O$, and (6)* $+ 2H_2O$ at potential of 0 V (a) and 0.8 V (b) relative to the computational[41] hydrogen electrode. The ideal pathway (shown in black) gives a flat line at 1.23 V, the ORR thermodynamic reversible potential. The Fe, N, C, and H atoms are represented by yellow, blue, brown, and white spheres, respectively.

fifth ligand onto $FeCoN_5$, which decreases subsequent binding energies of ORR intermediates.[20] Our DFT calculations also agree with the experimental results reported by Cao *et al.*,[39] which show that the FePc anchored on pyridine-functionalized carbon nanotubes (FePc−Py−CNTs) featured with the NH_2-Fe-N_4 structure exhibits much higher ORR activity as compared with the FePc directly anchored on CNTs (FePc-CNTs) featured with in-plane $Fe-N_4$ structure. In addition to optimizing the binding energies of ORR intermediates, the Fe displacement induced by the fifth axial ligand may facilitate O_2 adsorption via reducing the number of d_z^2-electrons of the central Fe (Supporting Information Figure S9 and Table S4), given that the completely filled d_z^2 orbital of D2 prevents the end-on adsorption of molecular oxygen.[14]

Therefore, one way to increase the ORR activity of iron-based catalysts is to selectively yield the D3 site. However, neither the formation mechanism of the D3 site nor the nature of the fifth axial ligand in the D3 site is clear. Given the three-dimensional (3-D) nature of this site and the absence of this site in Fe-macrocycle-pyrolyzed catalysts, it is inferred that the D3 site resides in 3-D micropores derived from the highly microporous carbon material (PANI here), and the D3 content increases with increase of the 3-D micropore population. Plausible evidence of this hypothesis is that the D3 content in the $Fe-N_x-C$

catalyst was significantly increased by replacing the Black Pearls 2000 to zeolitic-imidazolate-framework enriched with 3D micropores, with a consequence of ORR activity increase.[3,28] In addition, a prior report by Holby et al.,[20] using DFT calculations, suggests that the *OH may serve as a fifth ligand responsible for the displacement of the central Fe, thereby accounting for the higher ORR rate. The clarification of the fifth axial ligand may advance the development of non-PGM catalysts and the fundamental understanding of the ORR kinetics mediated by metal–nitrogen coordinate centers.

CONCLUSION

We show that the new active sites (D1 and D3) in pyrolyzed Fe–N$_x$–C catalysts exhibit distinctly different Fe displacements and Fe–N switching behaviors during ORR from the original Fe–N$_4$ macrocycle (D2), which accounts for their enhanced ORR activity. The new principles linking the dynamic structure of M–N$_x$–C sites during chemical reactions to catalytic activity are expected to be applicable to a broad variety of transition-metal compounds such as oxides, nitrides, chalcogenides, and metalloporphyrins, and potentially guide rational design of these non-PGM materials for broad applications.

METHODS

Catalyst Preparation. Iron(III) *meso*-tetraphenylporphyrin chloride (FeTPPCl) (Alfa Aesar) was mixed with Black Pearl carbon (BP) in the mass ratio 1:4 and ball milled for 2 h at 400 rpm, followed by pyrolysis at 300–800 °C under argon atmosphere. There is some carbon and nitrogen loss in the precursor mix during pyrolysis. The loading of iron in the pyrolyzed catalysts, including both complexed iron and/or metallic iron forms, was typically ~3% by weight as determined by energy dispersive analysis of X-rays and inductively coupled plasma mass spectrometry (ICP-MS).[6] Detailed informaion on the preparation and pyrolysis process of polyaniline Fe (PANI–Fe–C) was given in other recent work.[2,48] In brief, a short-chain aniline oligomer was mixed with high-surface area carbon material (pristine Ketjenblack EC-300J) and transition metal precursors (iron(III) chloride), followed by the addition of ammonium persulfate to fully polymerize the aniline. After vacuum-drying, the remaining solid material underwent a heat treatment at 900 °C in N$_2$ atmosphere, and then leached in 0.5 M H$_2$SO$_4$ at 80 °C for 8 h. The preleached catalyst was subjected to another heat treatment under N$_2$ atmosphere. The initial Fe content in the precursor was chosen to be 3.3 wt % here, and the changes of the Fe content during the synthesis and heat treatments is provided in a previous study.[48]

Electrochemical Measurements. All electrochemical measurements were made at room temperature using a rotating disk electrode (RDE) setup (Supporting Information Figure S10). Catalyst inks were prepared by ultrasonically dispersing the catalyst powder in a 1:1 (by volume) ratio of water/isopropanol solution. Typical catalyst loadings employed were 100 μg/cm^2 catalyst on a 5.61 mm glassy carbon disk. Reversible hydrogen electrode (RHE) generated using the same electrolyte as the bulk was used as the reference electrode. The gold ring electrode was held at 1.1 V vs RHE in alkaline electrolyte and at 1.3 V vs RHE in acidic electrolyte to detect stable peroxide intermediate. Square-wave voltammetry experiments were performed using a step potential of 5 mV, potential amplitude of 20 mV, and a scan frequency of 10 Hz. Britton–Robinson buffer solutions were used for electrochemical experiments performed at electrolyte pH ranging from 2 to 12. For these pH conditions from 2 to 12, a Ag/AgCl reference electrode prepared in saturated sodium chloride was utilized for the experiments.

X-ray Absorption Spectroscopic (XAS) Measurements. The *in situ* XAS studies were performed at the X3B beamline of the National Synchrotron Light Source (NSLS, Brookhaven National Laboratory, NY). A detailed description of the *in situ* spectro-electrochemical cell design is given elsewhere.[49] Spectra at Fe K-edge were collected in fluorescence mode using a 32-elements GE solid state dectector. Measurements were performed at different electrode potentials from 0.1 to 1.0 V (or higher) vs RHE (all the potentials mentioned in this paper are versus RHE unless otherwise specified). Details of electrochemical procedure associated with the *in situ* XAS measurements, and the XAS data analysis are provided in the Supporting Information.

FEFF Calculations. The FEFF9 program, an *ab initio* real space multiple-scattering (RSMS) code that employs full multiple scattering self-consistent field (SCF) calculations,[50] has been demonstrated to be suitable for mimicking the hybridization between the 4s and 4p states of iron and the symmetry-adopted atomic orbitals of the surrounding atoms in Fe-based complexes.[28,51] The Fe–N$_4$-C$_8$ with two atomic shells centered on the Fe atom (Figure 2b, inset), which can be considered as the common part of the three cluster models (Fe–N$_4$–C$_{12}$, Fe–N$_4$–C$_{10}$, and Fe–N$_4$–C$_8$) used in our previous work[6] for $\Delta\mu$ analysis, was chosen for XANES calculations. The shells further away were not included for FEFF calculations as the XANES spectral lines of Fe-based composites are dominated by shells located at distances of less than 4 Å.[28] The cluster structure was tuned by displacing the central Fe atoms out of the N$_4$-plane with a variety of Fe–N bond lengths to evaluate the central Fe displacement effects on the XAENS spectra.

DFT Calculations. The DFT calculations were performed using the Vienna *ab initio* Simulation Package (VASP)[52] with the projector augmented wave (PAW)[53] implementation. The exchange and correlation potential was calculated within the generalized gradient approximation (GGA)[54] since gradient corrections to the local spin density approximation are crucial in order to describe correctly the magnetic properties of iron.[55] Three clusters Fe–N4–Cx (x = 8, 10, 12) were modeled using a 4 × 6 graphene cluster (Supporting Information Figure S6). The details of the calculations are provided in the Supporting Information.

Conflict of Interest: The authors declare no competing financial interest.

Supporting Information Available: The Supporting Information is available free of charge on the ACS Publications website at DOI: 10.1021/acsnano.5b05984.

EXAFS and XANES analysis, FEFF calculations, DFT calculations, and RDE testing results (PDF)

REFERENCES AND NOTES

1. Lefèvre, M.; Proietti, E.; Jaouen, F.; Dodelet, J.-P. Iron-Based Catalysts with Improved Oxygen Reduction Activity in Polymer Electrolyte Fuel Cells. *Science* **2009**, *324*, 71–74.

2. Wu, G.; More, K. L.; Johnston, C. M.; Zelenay, P. High-Performance Electrocatalysts for Oxygen Reduction Derived from Polyaniline, Iron, and Cobalt. *Science* **2011**, *332*, 443–447.

3. Proietti, E.; Jaouen, F.; Lefèvre, M.; Larouche, N.; Tian, J.; Herranz, J.; Dodelet, J.-P. Iron-Based Cathode Catalyst with Enhanced Power Density in Polymer Electrolyte Membrane Fuel Cells. *Nat. Commun.* **2011**, *2*, 416.

4. Sabatier, P. Hydrogénations et Déshydrogénations par Catalyse. *Ber. Dtsch. Chem. Ges.* **1911**, *44*, 1984–2001.

5. Calle-Vallejo, F.; Martinez, J. I.; Rossmeisl, J. Density Functional Studies of Functionalized Graphitic Materials with Late Transition Metals for Oxygen Reduction Reactions. *Phys. Chem. Chem. Phys.* **2011**, *13*, 15639–15643.

6. Ramaswamy, N.; Tylus, U.; Jia, Q.; Mukerjee, S. Activity Descriptor Identification for Oxygen Reduction on Non-precious Electrocatalysts: Linking Surface Science to Coordination Chemistry. *J. Am. Chem. Soc.* **2013**, *135*, 15443–15449.

7. Tylus, U.; Jia, Q.; Strickland, K.; Ramaswamy, N.; Serov, A.; Atanassov, P.; Mukerjee, S. Elucidating Oxygen Reduction Active Sites in Pyrolyzed Metal—Nitrogen Coordinated Non-Precious-Metal Electrocatalyst Systems. *J. Phys. Chem. C* **2014**, *118*, 8999–9008.

8. Zagal, J.; Páez, M.; Silva, J. F. In *N4-Macrocyclic Metal Complexes*; Zagal, J., Bedioui, F., Dodelet, J.-P., Eds.; Springer: New York, 2006; pp 41–82.

9. Scherson, D. A.; Yao, S. B.; Yeager, E. B.; Eldridge, J.; Kordesch, M. E.; Hoffman, R. W. *In Situ* and *Ex Situ* Moessbauer Spectroscopy Studies of Iron Phthalocyanine Adsorbed on High Surface Area Carbon. *J. Phys. Chem.* **1983**, *87*, 932–943.

10. Bagotzky, V. S.; Tarasevich, M. R.; Radyushkina, K. A.; Levina, O. A.; Andrusyova, S. I. Electrocatalysis of the Oxygen Reduction Process on Metal Chelates in Acid Electrolyte. *J. Power Sources* **1978**, *2*, 233–240.

11. Schulenburg, H.; Stankov, S.; Schünemann, V.; Radnik, J.; Dorbandt, I.; Fiechter, S.; Bogdanoff, P.; Tributsch, H. Catalysts for the Oxygen Reduction from Heat-Treated Iron(III) Tetramethoxyphenylporphyrin Chloride: Structure and Stability of Active Sites. *J. Phys. Chem. B* **2003**, *107*, 9034–9041.

12. Koslowski, U. I.; Abs-Wurmbach, I.; Fiechter, S.; Bogdanoff, P. Nature of the Catalytic Centers of Porphyrin-Based Electrocatalysts for the ORR: a Correlation of Kinetic Current Density with the Site Density of $Fe-N_4$ Centers. *J. Phys. Chem. C* **2008**, *112*, 15356–15366.

13. Kramm, U. I.; Abs-Wurmbach, I.; Herrmann-Geppert, I.; Radnik, J.; Fiechter, S.; Bogdanoff, P. Influence of the Electron-Density of FeN_4-Centers towards the Catalytic Activity of Pyrolyzed FeTMPPCl-Based ORR-Electrocatalysts. *J. Electrochem. Soc.* **2011**, *158*, B69–B78.

14. Kramm, U. I.; Herranz, J.; Larouche, N.; Arruda, T. M.; Lefevre, M.; Jaouen, F.; Bogdanoff, P.; Fiechter, S.; Abs-Wurmbach, I.; Mukerjee, S.; Dodelet, J.-P. Structure of the Catalytic Sites in Fe/N/C-Catalysts for O_2-Reduction in PEM Fuel Cells. *Phys. Chem. Chem. Phys.* **2012**, *14*, 11673–11688.

15. Kramm, U. I.; Lefèvre, M.; Larouche, N.; Schmeisser, D.; Dodelet, J.-P. Correlations between Mass Activity and Physicochemical Properties of Fe/N/C Catalysts for the ORR in PEM Fuel Cell via ^{57}Fe Mössbauer Spectroscopy and Other Techniques. *J. Am. Chem. Soc.* **2014**, *136*, 978–985.

16. Zitolo, A.; Goellner, V.; Armel, V.; Sougrati, M.-T.; Mineva, T.; Stievano, L.; Fonda, E.; Jaouen, F. Identification of Catalytic Sites for Oxygen Reduction in Iron- and Nitrogen-Doped Graphene Materials. *Nat. Mater.* **2015**, *14*, 937–942.

17. Szakacs, C. E.; Lefevre, M.; Kramm, U. I.; Dodelet, J.-P.; Vidal, F. A Density Functional Theory Study of Catalytic Sites for Oxygen Reduction in Fe/N/C Catalysts Used in H_2/O_2 Fuel Cells. *Phys. Chem. Chem. Phys.* **2014**, *16*, 13654–13661.

18. Holby, E. F.; Taylor, C. D. Control of Graphene Nanoribbon Vacancies by Fe and N Dopants: Implications for Catalysis. *Appl. Phys. Lett.* **2012**, *101*, 064102.

19. Holby, E. F.; Wu, G.; Zelenay, P.; Taylor, C. D. Structure of $Fe-N_x-C$ Defects in Oxygen Reduction Reaction Catalysts from First-Principles Modeling. *J. Phys. Chem. C* **2014**, *118*, 14388–14393.

20. Holby, E. F.; Taylor, C. D. Activity of N-coordinated Multi-Metal-Atom Active Site Structures for Pt-Free Oxygen Reduction Reaction Catalysis: Role of *OH Ligands. *Sci. Rep.* **2015**, *5*, 9286.

21. Dodelet, J.-P. In *N₄-Macrocyclic Metal Complexes*; Zagal, J., Bedioui, F., Dodelet, J.-P., Eds.; Springer: New York, 2006; pp 83–147.

22. Scheidt, W. R.; Reed, C. A. Spin-State/Stereochemical Relationships in Iron Porphyrins: Implications for the Hemoproteins. *Chem. Rev.* **1981**, *81*, 543–555.

23. Jorissen, K.; Rehr, J. J. New Developments in FEFF: FEFF9 and JFEFF. *Journal of Physics. J. Phys.: Conf. Ser.* **2013**, *430*, 012001.

24. Kim, S.; Tryk, D.; Bae, I. T.; Sandifer, M.; Carr, R.; Antonio, M. R.; Scherson, D. A. *In Situ* Extended X-Ray Absorption Fine Structure of an Iron Porphyrin Irreversibly Adsorbed on an Electrode Surface. *J. Phys. Chem.* **1995**, *99*, 10359–10364.

25. Stefan, I. C.; Mo, Y.; Ha, S. Y.; Kim, S.; Scherson, D. A. *In Situ* Fe K-Edge X-Ray Absorption Fine Structure of a Nitrosyl Adduct of Iron Phthalocyanine Irreversibly Adsorbed on a High Area Carbon Electrode in an Acidic Electrolyte. *Inorg. Chem.* **2003**, *42*, 4316–4321.

26. Bae, I. T.; Tryk, D. A.; Scherson, D. A. Effect of Heat Treatment on the Redox Properties of Iron Porphyrins Adsorbed on High Area Carbon in Acid Electrolytes: an *In Situ* Fe K-Edge X-ray Absorption Near-Edge Structure Study. *J. Phys. Chem. B* **1998**, *102*, 4114–4117.

27. Boillot, M.-L.; Zarembowitch, J.; Itie, J.-P.; Polian, A.; Bourdet, E.; Haasnoot, J. G. Pressure-Induced Spin-State Crossovers at Room Temperature in Iron(II) Complexes: Comparative Analysis; a XANES Investigation of Some New Transitions. *New J. Chem.* **2002**, *26*, 313–322.

28. Briois, V.; Sainctavit, P.; Long, G. J.; Grandjean, F. Importance of Photoelectron Multiple Scattering in the Iron K-Edge X-Ray Absorption Spectra of Spin-Crossover Complexes: Full Multiple Scattering Calculations for Several Iron(II) Trispyrazolylborate and Trispyrazolylmethane Complexes. *Inorg. Chem.* **2001**, *40*, 912–918.

29. Hannay, C.; Hubin-Franskin, M.-J.; Grandjean, F.; Briois, V.; Polian, A.; Trofimenko, S.; Long, G. J. X-Ray Absorption Spectroscopic Study of the Temperature and Pressure Dependence of the Electronic Spin States in Several Iron(II) and Cobalt(II) Tris(pyrazolyl)borate Complexes. *Inorg. Chem.* **1997**, *36*, 5580–5588.

30. Khalil, M.; Marcus, M. A.; Smeigh, A. L.; McCusker, J. K.; Chong, H. H. W.; Schoenlein, R. W. Picosecond X-Ray Absorption Spectroscopy of a Photoinduced Iron(II) Spin Crossover Reaction in Solution. *J. Phys. Chem. A* **2006**, *110*, 38–44.

31. Natoli, C. R. In *EXAFS and near edge structure III*; Hodgson, K., Hedman, B., Penner-Hahn, J., Eds.; Springer: Berlin, Heidelberg, 1984; Vol. 2, pp 38–42.

32. Ramaswamy, N.; Mukerjee, S. Fundamental Mechanistic Understanding of Electrocatalysis of Oxygen Reduction on Pt and Non-Pt Surfaces: Acid *versus* Alkaline Media. *Adv. Phys. Chem.* **2012**, *2012*, 491604.

33. Deng, D.; Yu, L.; Chen, X.; Wang, G.; Jin, L.; Pan, X.; Deng, J.; Sun, G.; Bao, X. Iron Encapsulated within Pod-like Carbon Nanotubes for Oxygen Reduction Reaction. *Angew. Chem., Int. Ed.* **2013**, *52*, 371–375.

34. Hu, Y.; Jensen, J. O.; Zhang, W.; Cleemann, L. N.; Xing, W.; Bjerrum, N. J.; Li, Q. Hollow Spheres of Iron Carbide Nanoparticles Encased in Graphitic Layers as Oxygen Reduction Catalysts. *Angew. Chem., Int. Ed.* **2014**, *53*, 3675–3679.

35. Strickland, K.; Miner, E.; Jia, Q.; Tylus, U.; Ramaswamy, N.; Liang, W.; Sougrati, M.-T.; Jaouen, F.; Mukerjee, S. Highly Active Oxygen Reduction Non-Platinum Group Metal Electrocatalyst without Direct Metal-Nitrogen Coordination. *Nat. Commun.* **2015**, *6*, 7343.

36. Bouwkamp-Wijnoltz, A. L.; Visscher, W.; van Veen, J. A. R.; Boellaard, E.; van der Kraan, A. M.; Tang, S. C. On Active-Site Heterogeneity in Pyrolyzed Carbon-Supported Iron Porphyrin Catalysts for the Electrochemical Reduction of Oxygen: an *In Situ* Mössbauer Study. *J. Phys. Chem. B* **2002**, *106*, 12993–13001.

37. Scherson, D.; Tanaka, A. A.; Gupta, S. L.; Tryk, D.; Fierro, C.; Holze, R.; Yeager, E. B.; Lattimer, R. P. Transition Metal Macrocycles Supported on High Area Carbon: Pyrolysis—Mass Spectrometry Studies. *Electrochim. Acta* **1986**, *31*, 1247–1258.

38. Ferrandon, M.; Kropf, A. J.; Myers, D. J.; Artyushkova, K.; Kramm, U.; Bogdanoff, P.; Wu, G.; Johnston, C. M.; Zelenay, P. Multitechnique Characterization of a Polyaniline—Iron—Carbon Oxygen Reduction Catalyst. *J. Phys. Chem. C* **2012**, *116*, 16001–16013.

39. Cao, R.; Thapa, R.; Kim, H.; Xu, X.; Gyu Kim, M.; Li, Q.; Park, N.; Liu, M.; Cho, J. Promotion of Oxygen Reduction by a Bio-Inspired Tethered Iron Phthalocyanine Carbon Nanotube-Based Catalyst. *Nat. Commun.* **2013**, *4*, 2076.

40. Anderson, A. B.; Sidik, R. A. Oxygen Electroreduction on FeII and FeIII Coordinated to N_4 Chelates. Reversible Potentials for the Intermediate Steps from Quantum Theory. *J. Phys. Chem. B* **2004**, *108*, 5031–5035.

41. Nørskov, J. K.; Rossmeisl, J.; Logadottir, A.; Lindqvist, L.; Kitchin, J. R.; Bligaard, T.; Jónsson, H. Origin of the Over-potential for Oxygen Reduction at a Fuel-Cell Cathode. *J. Phys. Chem. B* **2004**, *108*, 17886–17892.

42. Jia, Q.; Caldwell, K.; Ziegelbauer, J. M.; Kongkanand, A.; Wagner, F. T.; Mukerjee, S.; Ramaker, D. E. The Role of OOH Binding Site and Pt Surface Structure on ORR Activities. *J. Electrochem. Soc.* **2014**, *161*, F1323–F1329.

43. Roth, C.; Benker, N.; Buhrmester, T.; Mazurek, M.; Loster, M.; Fuess, H.; Koningsberger, D. C.; Ramaker, D. E. Determination of O[H] and CO Coverage and Adsorption Sites on PtRu Electrodes in an Operating PEM Fuel Cell. *J. Am. Chem. Soc.* **2005**, *127*, 14607–14615.

44. Lewis, E. A.; Segre, C. U.; Smotkin, E. S. Embedded Cluster Δ-XANES Modeling of Adsorption Processes on Pt. *Electrochim. Acta* **2009**, *54*, 7181–7185.

45. Gottesfeld, S. Generation of Active Sites by Potential-Driven Surface Processes: A Central Aspect of Electrocatalysis. *ECS Trans.* **2014**, *61*, 1–13.

46. Studt, F. The Oxygen Reduction Reaction on Nitrogen-Doped Graphene. *Catal. Lett.* **2013**, *143*, 58–60.

47. Kattel, S.; Wang, G. A Density Functional Theory Study of Oxygen Reduction Reaction on Me-N_4 (Me = Fe, Co, or Ni) Clusters between Graphitic Pores. *J. Mater. Chem. A* **2013**, *1*, 10790–10797.

48. Wu, G.; Johnston, C. M.; Mack, N. H.; Artyushkova, K.; Ferrandon, M.; Nelson, M.; Lezama-Pacheco, J. S.; Conradson, S. D.; More, K. L.; Myers, D. J.; Zelenay, P. Synthesis-Structure-Performance Correlation for Polyaniline-Me-C Non-Precious Metal Cathode Catalysts for Oxygen Reduction in Fuel Cells. *J. Mater. Chem.* **2011**, *21*, 11392–11405.

49. Arruda, T. M.; Shyam, B.; Lawton, J. S.; Ramaswamy, N.; Budil, D. E.; Ramaker, D. E.; Mukerjee, S. Fundamental Aspects of Spontaneous Cathodic Deposition of Ru onto Pt/C Electrocatalysts and Membranes under Direct Methanol Fuel Cell Operating Conditions: an *In Situ* X-Ray Absorption Spectroscopy and Electron Spin Resonance Study. *J. Phys. Chem. C* **2010**, *114*, 1028–1040.

50. Ankudinov, A. L.; Ravel, B.; Rehr, J. J.; Conradson, S. D. Real-Space Multiple-Scattering Calculation and Interpretation of X-Ray-Absorption Near-Edge Structure. *Phys. Rev. B: Condens. Matter Mater. Phys.* **1998**, *58*, 7565–7576.

51. Briois, V.; dit Moulin, C. C.; Sainctavit, P.; Brouder, C.; Flank, A. M. Full Multiple Scattering and Crystal Field Multiplet Calculations Performed on the Spin Transition FeII(phen)$_2$(NCS)$_2$ Complex at the Iron K and L$_{2,3}$ X-Ray Absorption Edges. *J. Am. Chem. Soc.* **1995**, *117*, 1019–1026.

52. Kresse, G.; Furthmüller, J. Efficient Iterative Schemes for Ab Initio Total-Energy Calculations Using a Plane-Wave Basis Set. *Phys. Rev. B: Condens. Matter Mater. Phys.* **1996**, *54*, 11169–11186.

53. Blöchl, P. Projector Augmented-Wave Method. *Phys. Rev. B: Condens. Matter Mater. Phys.* **1994**, *50*, 17953–17979.

54. Perdew, J.; Burke, K.; Ernzerhof, M. Generalized Gradient Approximation Made Simple. *Phys. Rev. Lett.* **1996**, *77*, 3865–3868.

55. Barbiellini, B.; Moroni, E. G.; Jarlborg, T. Effects of Gradient Corrections on Electronic Structure in Metals. *J. Phys.: Condens. Matter* **1990**, *2*, 7597.